

Machine-learning semi-local exchange-correlation functionals for Kohn-Sham density functional theory of the Hubbard model

Eoghan Cronin^{1,*}, Rajarshi Tiwari^{1,2,†} and Stefano Sanvito^{1‡}

¹ *School of Physics, AMBER and CRANN Institute, Trinity College, Dublin 2, Ireland*

² *Irish Centre for High-End Computing (ICHEC), University of Galway, Ireland.*

(Dated: January 29, 2025)

The Hubbard model provides a test bed to investigate the complex behaviour arising from electron-electron interaction in strongly-correlated systems and naturally emerges as the foundation model for lattice density functional theory (DFT). Similarly to conventional DFT, lattice DFT computes the ground-state energy of a given Hubbard model, by minimising a universal energy functional of the on-site occupations. Here we use machine learning to construct a class of scalable ‘semi-local’ exchange-correlation functionals with an arbitrary degree of non-locality for the one-dimensional spinfull Hubbard model. Then, by functional derivative we construct an associated Kohn-Sham potential, that is used to solve the associated Kohn-Sham equations. After having investigated how the accuracy of the semi-local approximation depends on the degree of non-locality, we use our Kohn-Sham scheme to compute the polarizability of linear chains, either homogeneous or disordered, approaching the thermodynamic limit.

I. INTRODUCTION

Over the last few decades, density functional theory (DFT) has become the computational method of choice across several different fields, going from quantum chemistry to material science. Today, DFT serves as the primary tool for calculating the electronic structure of both solids and molecules, thanks to its foundation in the rigorously established Hohenberg-Kohn theorems [1], to the practical Kohn-Sham functional-minimization scheme [2], and to the numerous available efficient numerical implementations [3]. The Hohenberg-Kohn theorems establish the existence of a universal energy functional, $F[n]$, of the electron charge density, $n(\mathbf{r})$, functional that presents its minimum at the ground-state density. Thus, in principle, one can solve any ground-state electronic quantum-mechanics problem, by simply scanning through all the legitimate charge densities, in the search of the functional minimum. This conceptually simple strategy, known as orbital-free DFT [4], is however practically impossible.

Two main obstacles prevent the direct minimization of $F[n]$. Firstly, the exact functional is unknown, so that an exact solution of the problem is not available. This is partially mitigated by the possibility to break the functional into three contributions, (i) the kinetic energy of a non-interacting system having the same density, $T_0[n]$, (ii) the classical Coulomb energy (Hartree energy) and (iii) the so-called exchange-correlation energy, $E_{xc}[n]$. This last term describes the non-classical electron-electron interaction and the correction to the non-interacting kinetic energy arising from electron correlation. Importantly, there are many approximations to $E_{xc}[n]$ that allows one to perform accurate calculations. Hence, the

DFT problem, at least in an approximated form, is solvable. Yet, orbital-free DFT remains challenging, since the exact density-functional form for the non-interacting kinetic energy is unknown and there are no accurate and universal approximations for it working across different external potentials.

As a consequence, practically any numerical implementation of DFT follows the Kohn-Sham (KS) procedure. This consists in mapping the interacting many-body problem onto a fictitious single-particle one where, by construction, the two problems share the same ground-state energy and density. The potential associated to the single-particle problem is constructed from $F[n]$ by functional derivative and it is itself density dependent. As such, the non-interacting kinetic energy is computed exactly, but the solution of the KS equations must be iterative. Although, in principle, the exact functional depends on the electron density everywhere in space, namely it is non-local, the most common approximations to $E_{xc}[n]$ are local or semilocal. For instance, the local density approximation (LDA) assigns the exchange-correlation energy at a given point to that of the homogeneous electron gas computed for the density at that point [2]. More sophisticated and accurate approximations can then be constructed by expanding the functional dependence of the exchange-correlation energy to the density gradient and higher derivatives, following a systematic Jacob’s ladder [5]. These work well across a broad range of electronic-structure types, but they usually fail for systems presenting strongly correlated electrons [6]. The systematic construction of non-local functionals that satisfy the known conditions of exact DFT is highly non-trivial and their deployment in calculations for real systems is extremely numerically demanding.

Some of these challenges motivated the construction of DFT for lattice models, namely of lattice density functional theory (LDFT) [7, 8]. To fix the idea, let us consider the one-dimensional (1D) single-orbital Hubbard model [9]. LDFT then translates the Hohenberg-Kohn

* eoghanc@tcd.ie

† rajarshi.tiwari@ichec.ie

‡ sanvitos@tcd.ie

theorems by replacing the electron density with the site occupation. One can then define a universal functional that depends on the entire occupation manifold, namely on the average occupation of each site comprising the model. Although one should be careful to transfer DFT concepts to LDFT [10–13], the study of lattice models has a number of advantages. In particular, in LDFT the charge density has a simple single representation, some exact limiting solutions are known [14], and, for relatively small systems, exact numerical results can be obtained at a moderate computational cost. As such, LDFT can be seen as a simple playground to investigate some fundamental questions of DFT. For instance, by using the Bethe ansatz solution of the Hubbard model one can construct LDA functionals [15, 16] and then investigate the response of strongly correlated systems to electric [17] and magnetic fields [18], their susceptibility [19], the formation of the Mott gap [20] and quantum transport [21].

An interesting aspect of any functional theory is given by the possibility of combining it with machine-learning (ML) techniques. In fact, within conventional DFT, ML appears ideal to construct numerical mappings between the electron density and the energy [22–29], between the external potential and the electron density [30–32], between the electron density and the ground-state wave function [33] or between the electron density and an observable [34]. Moving to lattice models, we have shown that a numerically exact functional can be constructed for the spin-full Hubbard model in one dimension [35]. This depends on the site occupations of the entire system, namely it is a fully non-local functional, and it satisfies both Hohenberg-Kohn theorems. Unfortunately, since the energy depends on the entire site occupation manifold, a functional trained on a N -site system cannot be used to predict the energy of systems of other size. We have then avoided such drawbacks by constructing semi-local ML functionals, this time for the spinless Hubbard model [36]. In both of these two examples, the energy minimization is performed in an orbital-free-DFT fashion.

In this work, we take an alternative approach, namely we demonstrate that a Kohn-Sham potential for the spin-full 1D Hubbard model can be obtained from the numerical ML energy functional by functional derivative. This is constructed semi-locally so that it can be trained on relatively small systems and then used for much larger ones. With this, we are able to investigate relevant quantities as they approach the thermodynamic limit, namely for a large number of sites. In particular, we concentrate here on the charge density response of the one-dimensional Hubbard model in the metallic state and in the presence of disorder, for which we evaluate the polarizability.

The paper is structured as follows. In Section II we present our methodology, by setting up the problem, discussing how to generate the target data set, and by explaining how we train the ML functional. Our presentation of the results begins in Section III A by demonstrating the performance of our KS equations and the

accuracy of the constructed KS potential. This is followed by an analysis of the non-locality of the functional in Section III B. We then proceed to look at some applications of the trained functional. In Sec. III C we apply it to solve systems with a filling factor outside the range used for the training. Then, we analyze the (deviation from) piecewise-linearity of the energy at fractional electron filling and the associated derivative discontinuity [see Section III D]. Finally, in Section III E we investigate the response of the charge density to an electric field and the ability of the model to solve systems with thousands of lattice sites. Conclusions are drawn in Section IV.

II. METHOD

A. Kohn-Sham LDFT setup for Hubbard model

Our analysis is based on the one-dimensional, single-orbital, spin-full Hubbard model [9], described by the following Hamiltonian,

$$\hat{H}_U = \hat{T} + \hat{U} + \sum_{i\sigma} v_i \hat{n}_{i\sigma}. \quad (1)$$

This comprises the kinetic energy,

$$\hat{T} = -t \sum_{i\sigma} \left(\hat{c}_{i\sigma}^\dagger \hat{c}_{i+1,\sigma} + \hat{c}_{i+1,\sigma}^\dagger \hat{c}_{i\sigma} \right), \quad (2)$$

the electron-electron repulsion,

$$\hat{U} = U \sum_i \hat{n}_{i\uparrow} \hat{n}_{i\downarrow}, \quad (3)$$

and the external potential, defined through the set of on-site energies, $\{v_i\}$. Here $\hat{c}_{i\sigma}^\dagger$ ($\hat{c}_{i\sigma}$) is the fermionic creation (annihilation) operator for an electron at site i with spin $\sigma = \uparrow, \downarrow$, the $\hat{n}_{i\sigma} = \hat{c}_{i\sigma}^\dagger \hat{c}_{i\sigma}$ are the occupation operators, while t and $U > 0$ are the electronic hopping integral and the Coulomb repulsion energy, respectively.

The LDFT version of the Hohenberg-Kohn theorems [7, 8] establishes that there exists a universal functional, $F_U[\{n_{i\sigma}\}]$, of the spin-resolved site occupations, $n_{i\sigma} = \langle \hat{n}_{i\sigma} \rangle$, such that the total energy of the system, $E_U[\{n_{i\sigma}\}]$, can be written as

$$E_U[\{n_{i\sigma}\}] = F_U[\{n_{i\sigma}\}] + \sum_{i\sigma} n_{i\sigma} v_i, \quad (4)$$

where by definition,

$$F_U[\{n_{i\sigma}\}] = \langle \Psi[\{n_{i\sigma}\}] | \hat{T} + \hat{U} | \Psi[\{n_{i\sigma}\}] \rangle, \quad (5)$$

with $|\Psi[\{n_{i\sigma}\}]\rangle$ being the many-body wave function. Note that the functional depends on the Coulomb repulsion energy U (there is a different universal functional for every different U), and the $U = 0$ limit recovers the non-interacting tight-binding model. Thus, in analogy with

conventional DFT, one defines the exchange-correlation energy $E_{xc}[\{n_{i\sigma}\}]$, as

$$E_{xc}[\{n_{i\sigma}\}] = F_U[\{n_{i\sigma}\}] - F_{U=0}[\{n_{i\sigma}\}], \quad (6)$$

where, at variance with DFT, we have not singled out the classical Hartree contribution. With such definition at hand we can readily write down the associated KS equations as follows

$$(\hat{T} + v_{\text{eff},i\sigma})\phi_m = \epsilon_m \phi_m, \quad (7)$$

where $v_{\text{eff},i\sigma} = v_{xc,i\sigma} + v_i$ is the KS potential, while ϵ_m and ϕ_m are the KS energies and orbitals, respectively. Formally, the exchange-correlation potential is obtained as functional derivative of the corresponding energy, $v_{xc,i\sigma} = \frac{\partial E_{xc}}{\partial n_{i\sigma}}$, but in practice this is just a standard derivative, since E_{xc} is a function of the $2L$ -dimensional vector of site occupations, $\{n_{i\sigma}\}$, where L is the total number of sites.

Throughout this work, we will consider the case of one-third filling, $N_e/L = 2/3$ (N_e is the total number of electrons), which is representative of the metallic phase. Thus, we stay away from half-filling, corresponding to the Mott insulating phase, as this presents a much longer correlation length and it is usually much harder to converge. Furthermore, we look at finite-size chains with open boundary conditions and a net spin-zero state, namely at the situation $N_\uparrow = N_\downarrow = N_e/2$. In this case, spin symmetry allows us to drop the spin index and we will express all quantities in terms of the total occupation $n_i = n_{i\uparrow} + n_{i\downarrow}$.

B. Generation of the training and test sets

The construction of the ML exchange-correlation energy consists in establishing a mapping between the ground-state site occupations, $\{n_{i\sigma}\}$, and E_{xc} . As such, for a given set of on-site energies $\{v_i\}$ one needs to compute the exact ground-state energy of the system. The value of E_{xc} is then obtained by subtracting the contribution from the external potential [see Eq. (1)] and the kinetic energy of the non-interacting system [see Eq. (6)]. We use the density-matrix renormalization group (DMRG) [37] algorithm via TenPy [38] to solve the full many-body problem. Throughout this work, we fix the hopping parameter to $t = 1$, which sets the energy scale of the problem, and consider the case $U = 4$. The training set is constructed from data corresponding to lattice of different sizes, $L = 18, 21, 24$, and for each one of them we produce 17,000 data points.

In order to generate a dense and diverse training dataset, we use the following strategy. A data point here corresponds to a different choice of external potential, generated randomly within an interval $v_i^{(k)} \in [0, \lambda^{(k)}]$. In particular, for each lattice size, $n = 15,000$ configurations are obtained from $\lambda^{(k)} = \sqrt{9k/(n-1)}$. The first data point $\lambda^{(k=0)} = 0$ gives us the homogeneous

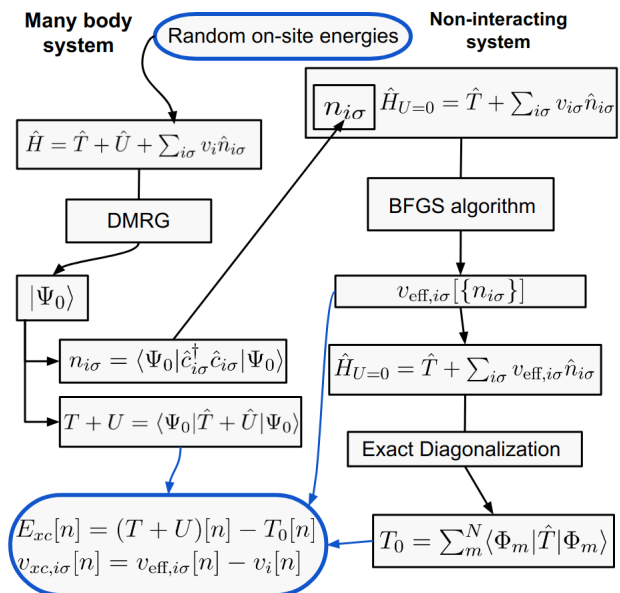


FIG. 1. Workflow of the generation of the ‘exact’ data. On the left-hand side we describe the DMRG pipeline. By starting with some random on-site-energy configuration, we use the DMRG algorithm to find the ground-state wavefunction, density and energy. The construction of the ‘exact’ KS potential is depicted on the right-hand side. The DMRG density is supplied to the BFGS algorithm, along with the non-interacting Hamiltonian to find the effective potential that reproduces the ground-state density. Finally, $E_{xc}[n]$ and $v_{xc,i}[n]$ are computed by subtraction (blue box).

case, while the final point gives $\lambda^{(k=14999)} = 3$. The square root dependence on k is selected as it gives rise to a good distribution of densities, as it pushes more of the data points further away from the homogeneous case. Then, we obtain a further $n = 2,000$ configurations from $\lambda^{(k)} = 3 + 3k/(n-1)$, a choice that guarantees enough diversity in the training set. Finally, we also include in the training dataset potentials obtained by applying constant electric fields of different strength [see Section III E] over the homogeneous lattice $v_i = 0$. The DMRG data are here deemed as ‘exact’, although their accuracy is limited by the DMRG calculation itself. Poorly converged DMRG data are not included in the training set. The threshold of accuracy was set by requiring that the relative change in the energy is within 10^{-5} after the final step.

As far as the test set is concerned, this is also generated by DMRG for a larger variety of lattice sizes, $L = 24, 30, 36, 42, 48, 54, 60$, with $n = 1,000$ random external potentials taken from $\lambda^{(k)} = \sqrt{9k/(n-1)}$. In this case, we do not reject any DMRG results, not to create bias in the test set, namely, we want to avoid biasing the test set towards some particular class of disorder configurations. Since one of the target quantities is the KS exchange-correlation potential obtained as the functional derivative of the corresponding energy, we also need to generate test data for v_{xc} . For this quantity we follow a

well-established reverse engineering strategy, sometimes known as the inverse-Kohn-Sham method [39]. This essentially consists of varying the effective potential until the targeted site occupations are obtained, namely those computed with DMRG. In practice, we minimize the Euclidean distance $\|n[v_{\text{eff}}] - n_{\text{DMRG}}\|$ and the convergence is set by a threshold of 10^{-5} . The same criterion is adopted for each lattice size investigated. In our case, we use the robust Broyden-Fletcher-Goldfarb-Shanno (BFGS) algorithm [40–43], as implemented in SciPy [44], to descend onto the effective potential that reproduces the DMRG density. The workflow of the data generation is presented in Fig. 1. All of our data and some examples of our code are publicly available on GitHub [45].

C. Machine-learning the functional

We have mentioned before, that our functional is constructed semi-local. This actually means that E_{xc} is obtained as the sum of site-dependent exchange-correlation energy densities e_{xc} , which in turn, depend on the occupation around that site within a given cutoff a , namely we have

$$E_{\text{xc}}^{\text{ML}}[n] = \sum_i^{L+2a} e_{\text{xc}}^{\text{ML}}[\bar{n}_{i,a}], \quad (8)$$

where $\bar{n}_{i,a} = (n_{i-a}, n_{i-a+1}, \dots, n_i, \dots, n_{i+a-1}, n_{i+a})$, and a is positive integer, which we call the non-locality parameter (cutoff radius). Note that the summation extends beyond indices associated to the actual lattice, since the non-locality assigns non-vanishing $\bar{n}_{i,a}$ vectors even when the index i is outside the lattice boundaries. Then, the ML KS potential at site i for spin σ , $v_{\text{xc},i\sigma}^{\text{ML}}$, is computed by summing up the partial derivative with respect to $n_{i\sigma}$ of all the energy-density terms that contain $n_{i\sigma}$

$$v_{\text{xc},i\sigma}^{\text{ML}}[n] = \frac{\partial}{\partial n_{i\sigma}} E_{\text{xc}}^{\text{ML}}[n] = \frac{\partial}{\partial n_{i\sigma}} \sum_j e_{\text{xc}}^{\text{ML}}[\bar{n}_{j,a}]. \quad (9)$$

The ML exchange-correlation energy is constructed as a fully connected neural network comprising five dense layers, each of 64 nodes, while the KS potential is obtained by the automatic differentiation as supplied by TensorFlow [46]. We choose the exponential linear unit as an activation function to ensure that the functional derivatives are continuous. In each case, we train for 5,000 epochs with the Adam optimizer and a batch size of 32. One neural network is trained for each value of the non-locality parameter explored $a = 1, 2, 3, 4$. The learning rate is decayed according to

$$\lambda(j) = \lambda_0 \left(\frac{1}{30} \right)^{j/5000} \quad (10)$$

where $\lambda_0 = 3 \cdot 10^{-4}$ and j is the epoch iteration. It is necessary to use zero-padding while computing the energy density near the boundary, as the non-local terms

extend beyond it. In the context of LDFT, the use of zero padding can be understood as follows. Our finite system of L -sites with open boundary conditions can be considered to lie in the infinite chain with the on-site energies given by

$$v_i = \begin{cases} v_i & \text{if } 0 \leq i < L \\ +\infty & \text{otherwise.} \end{cases} \quad (11)$$

Corresponding to these on-site energies, the densities will be

$$n_{i\sigma} = \begin{cases} n_{i\sigma}[\{v_i\}] & \text{if } 0 \leq i < L \\ 0 & \text{otherwise.} \end{cases} \quad (12)$$

Data from larger systems can be understood to lie on the same infinite chain, the only difference being that some on-site energies at the boundary are brought down from infinity, allowing electrons to access those sites. Moreover, this compliments the fact that the $\hat{T} + \hat{U}$ component of the Hamiltonian is invariant, so that the same density-functional is valid for different numbers of lattice sites.

III. RESULTS

A. Solving the Kohn-Sham Equations

Let us start our analysis by giving a simple demonstration of a successful implementation of the trained functional and how to use it. In Fig. 2 we present the site occupations and the converged KS exchange-correlation potential for a system of $L = 60$ sites and an external potential of the form $v_i = \cos\left(\frac{2\pi i}{L}\right) - \frac{1}{2} \cos\left(\frac{12\pi i}{L}\right)$. The functional in this case was trained over $L = 18, 21, 24$ sites and here we compare the results from our ML KS (MLKS) scheme and the ‘exact’ DMRG reference. The KS self-consistent cycle is performed with a simple linear-mixing scheme [47], in which the input set of site occupations at the $(k+1)$ -th iteration, n^{k+1} , is constructed as $n^{k+1} = (1-\lambda)n^k + \lambda n'^k$, where n'^k is the set of output occupations at iteration k . Here we set λ to decay from 0.03 to 0.005 over the first 2,000 iterations and then to remain constant at 0.005 should more iterations be required, and the convergence criterion is $\|n^k - n'^k\| < 10^{-5}$. As we can observe in Fig. 2, there is a good visual agreement between the MLKS-calculated quantities (occupations and potential) and the DMRG reference. In particular, v_{xc} appears to have the correct expected behaviour, namely it becomes more prominent in regions of high electron density, corresponding to minima of the external potential.

It is important to note that when assessing the accuracy of the KS scheme at convergence one has to consider that the error in the KS potential itself adds to that of the ground-state site occupations, which are determined by the potential through the self-consistent cycle. It is

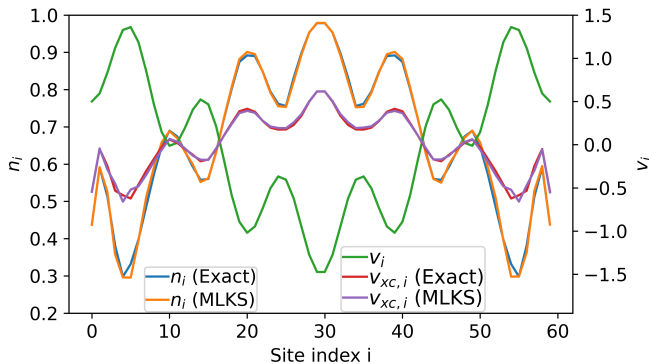


FIG. 2. The ground-state site occupations (left-hand side scale) and the exchange-correlation potential (right-hand side scale) obtained from the MLKS scheme are plotted alongside the exact DMRG results (denoted as ‘exact’). For this visual comparison we consider a $L = 60$ system and an external potential (green line) of the form $v_i = \cos\left(\frac{2\pi i}{L}\right) - \frac{1}{2} \cos\left(\frac{12\pi i}{L}\right)$.

then interesting to disentangle such errors by computing a number of additional quantities. In particular, in Fig 3 we compare both the exchange-correlation KS potential and energy density computed at either the exact DMRG density ($e_{xc}^{app}[n_{exact}]$ and $v_{xc}^{app}[n_{exact}]$, in panels (a) and (d), respectively) or the KS occupations ($e_{xc}^{app}[n_{KS}]$ and $v_{xc}^{app}[n_{KS}]$, in panels (b) and (e), respectively), with the corresponding exact (DMRG) quantities. Here, ‘app’ denotes the relevant approximate functional. Namely, our MLKS functional, or the fully-numerical implementation of the Bethe-ansatz LDA (BALDA) [8, 48–51]. The BALDA is perhaps the most developed non-ML approximation to the exchange-correlation functional for the Hubbard model. It can be used both in an orbital-free DFT mode or within a KS scheme. Here it will represent a point of comparison for our developed functional. For the results of Fig. 3 we consider a test system of 60 sites and the various parity plots are constructed over 1,000 disorder configurations.

In the case of MLKS, it appears that the error accumulated over the KS self-consistent cycle is only minor. In fact, we find a mean absolute (MAE) error over the exchange-correlation energy density of 2.2×10^{-4} , when this is computed at the exact DMRG occupations, a MAE that grows to only 3×10^{-4} with the converged KS occupations. Note that e_{xc}^{ML} averages at around 0.3 for this choice of disorder and occupation, meaning that the relative error on the energy density is of the order of 0.1%. Interestingly, the results for the KS exchange-correlation potential returns a situation where the MAE is lower, even if marginally when v_{xc}^{ML} is computed at the KS occupations rather than at the exact ones. This suggests that the functional derivative defining the KS potential may slightly shift the ground-state occupations from their exact values. In any case, an overall assessment of the model constructed can be obtained from panels (c) and (f) of Fig. 3, where we show the parity plot

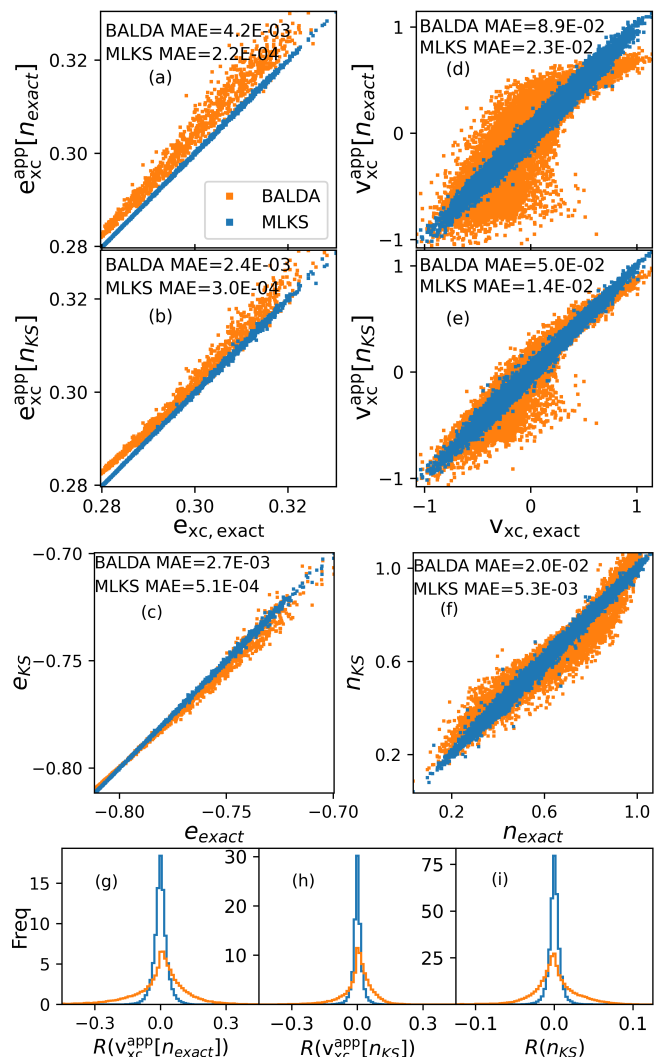


FIG. 3. Analysis of the accuracy of the MLKS and BALDA functionals. For a system of $L = 60$ sites, we present the parity plots of both the ML exchange-correlation energy density, e_{xc}^{app} , and the KS exchange-correlation potential, v_{xc}^{app} , computed either at the exact (DMRG) occupations [panels (a) and (d), respectively] or at the converged KS occupations, n_{KS} [panels (b) and (e), respectively]. The relevant approximate functional is denoted by ‘app’, and it corresponds to that indicated in the legend. In panels (c) and (f) we present the parity plots for the KS total energy density and occupations, respectively. Panels (g) and (h) display histograms of the residuals of v_{xc}^{app} at the exact and converged KS densities, and panel (i) shows the densities. Here, $R(x)$ denotes the residual quantity. For instance $R(n_{KS}) = n_{KS} - n_{exact}$. Results are presented for the MLKS functional with a non-locality parameter $a = 4$ and over a test set of 1,000 configurations. In the various panels we also report the MAE.

for the total energy density, $e_{MLKS} = F_U/L$ and the KS occupations, respectively. These give us relative MAEs of 0.07% (e_{MLKS}) and 1% (n), pointing to an extremely accurate model, whose main error accumulates in the self-consistent occupations.

Unlike the MLKS scheme, the BALDA results show some systematic error. Namely, e_{xc} appears to be over-approximated, while v_{xc} has some curvature relative to the parity line. Visually, the latter error [see Fig. 3 panels (d) through (f)] is inflated by the high number of data points on the plot, 60,000, where the majority of the points lie relatively close to the parity line, although they are not visible. Therefore, for a better visualization, we plot a histogram of the residuals in panels (g) through (i). Similarly to the case of MLKS, but to a much greater extent, the BALDA results improve dramatically, when computed at the converged KS density instead of the exact one. In fact, the errors on e_{xc} and v_{xc} drop roughly by a factor two. Furthermore, in panel (c) the systematic over-approximation of e_{xc} appears to be cancelled out by an under-approximation of the non-interacting kinetic energy, giving a e_{KS} in a satisfactory agreement with the exact data.

All considered, the MLKS functional appears to be in much better agreement with the exact functional than the well-known BALDA. The evidence for this is (i) the consistently lower values of MAE for each quantity, (ii) the absence of systematic errors in the parity plots and (iii) the higher degree of consistency between the results calculated at the exact and KS densities. In Appendix A, we repeat the same test, using the fully local $a = 0$ ML functional and discuss how that compares to the BALDA.

B. System size and non-locality parameter

In order to have a better insight into the ML functional construction, it is useful to investigate its non-local properties. The effects of the functional built-in non-locality are analysed by looking at lattice sizes ranging from 24 to 60, and by computing the MAEs for different values of the non-locality, $a = 1, 2, 3, 4$. The results ensemble-averaged over 1,000 disorder configurations are summarized in Fig 4, where we present the MAEs of $e_{xc}^{ML}[n_{exact}]$ and $e_{xc}^{ML}[n_{MLKS}]$ in panels (a) and (b), $v_{xc}^{ML}[n_{exact}]$ and $v_{xc}^{ML}[n_{MLKS}]$ in panels (d) and (e), and again the MAEs of $e_{MLKS} = F_U/L$ and the KS occupations in panels (c) and (f). A number of trends are clearly visible.

Firstly, one may notice that the functionals get progressively more accurate with increasing their non-locality a , in particular when going from $a = 1$ to $a = 3$, after which the performance improvement seems to saturate. This is particularly true for the energy density e_{xc}^{ML} , while further improvements at $a = 4$ are found for the potential v_{xc}^{ML} . Such numerical result indicates that the non-local correlation of the Hubbard model at the chosen filling factor is well captured at $a \simeq 3$. It is also interesting to note that the smaller MAE for v_{xc}^{ML} is computed at the MLKS occupations and not at the exact ones, $v_{xc}^{ML}[n_{exact}]$. This behaviour was observed before for $a = 4$ and it is found here for all systems regardless of the non-locality.

The second noteworthy trend is that, in general, the

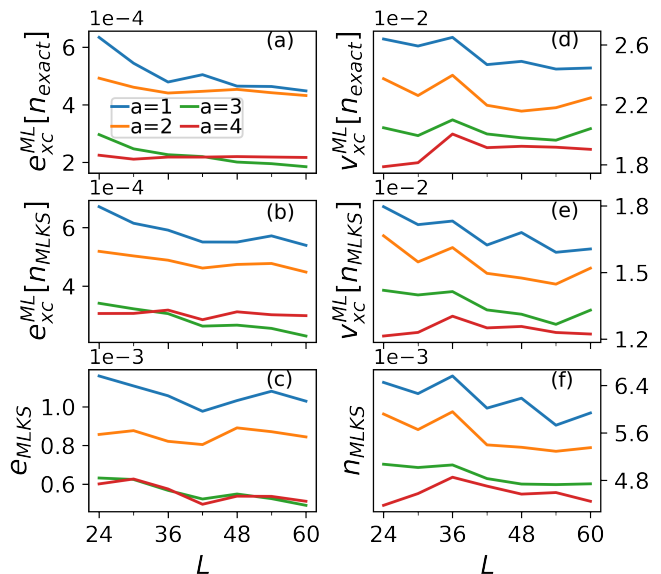


FIG. 4. The MAEs, computed over 1,000 disorder configurations for each system, as a function of the system size, L . Data are presented for the ML exchange-correlation energy density, e_{xc}^{ML} , and the KS exchange-correlation potential, v_{xc}^{ML} , computed either at the exact (DMRG) occupations [panels (a) and (d), respectively] or at the converged KS occupations [panels (b) and (e), respectively]. In panels (c) and (f) we present the MAE for the ML KS total energy density and occupations, respectively. In all cases, we show results for different values of the non-locality parameter a .

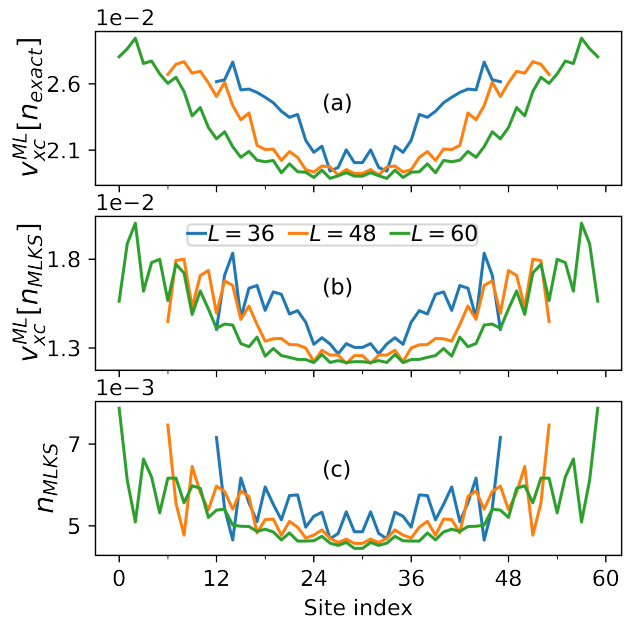


FIG. 5. Site-resolved MAE, computed over 1,000 disorder configurations for three lattice sizes, $L = 36, 48, 60$ and non-locality, $a = 4$. The (a) MAE for v_{xc}^{ML} at exact site occupations, n_{exact} , and (b) at the MLKS ones, n_{MLKS} . In panel (c) we show the MAE of the MLKS site occupations (see text for details).

MAE appears to decrease with increasing the lattice size. To investigate whether this is a boundary effect, we look into the site dependence of the MAEs as function of the lattice size. In Fig. 5 we show the site-resolved MAE of the KS exchange-correlation potential, computed at both the MLKS and exact occupations, and the final occupations, as a function of the lattice position. This is shown for three different lattices, $L = 36, 48$ and 60 , and the MAEs are averaged over 1,000 different disorder configurations. We find that, on average, the MAE at the edges of the lattice is about 25% larger than in the middle, suggesting that the systematic trend in the MAE decrease with system size may be due to a decreasing edge-to-bulk ratio. In contrast, in the middle of the lattice, all quantities converge to a similar MAE, regardless of the lattice size. The loss of accuracy at the lattice edges may be attributed to an imbalance in the training data. In fact, the edges are characterised by $\bar{n}_{i,a} = (n_{i-a}, n_{i-a+1}, \dots, n_i, \dots, n_{i+a-1}, n_{i+a})$ vectors presenting $n_j = 0$ for those sites lying outside the lattice. Vectors of this type, however, are less abundant in our training set. In fact, for a lattice of L sites and a non-local parameter a , there are $4a$ sites with $\bar{n}_{i,a}$ presenting at least one vanishing occupation and $L - 2a$ sites with all non-vanishing occupations.

In any case, our results return us a rather accurate exchange-correlation functional, which can be used to derive a KS potential via functional derivative. Already with a modest degree of non-locality, this allows us to compute energies and occupations close to those obtained with DMRG, with the accuracy improving as the system size grows.

C. Extrapolation to different filling factors

The universal DFT functional is independent of the total number of particles in the system. However, there is no guarantee that this property is transferred to approximated machine-learning formulations. Namely, although one can always extend a semi-local functional to filling factors outside the training range, it remains the question of whether the functional is actually accurate. This question naturally made us curious to test how well the trained functionals extrapolate to filling factors away from $2/3$. By using both the DMRG and the MLKS scheme, we now map the density, energy and exchange-correlation potential of 128 random configurations of a $L = 36$ lattice and different electron numbers, $N_e = 16, 18, \dots, 32$ (the training was performed for $N_e = 24$). In this test, we use the same $\lambda^{(k)} = \sqrt{9k/(n-1)}$ distribution described in Sec. II B to generate the disorder configurations, and examine how the average error depends on the number of electrons.

The results are given in Fig. 6. Unsurprisingly, the error minimizes at $N_e/L = \frac{2}{3}$, namely at the same filling of the training set, where all energies densities shown in panels (a) through (c) take on minima of the order

of 10^{-4} and have similar scaling away from this point. For instance, the converged Kohn-Sham energy density [panel (c), $a = 4$] has a MAE of 2×10^{-3} , 5×10^{-4} , 2×10^{-3} at $N_e = 18, 24$ and 30 , respectively. In the case of the exchange-correlation potential and similarly for the occupation, the MAE varies more slowly against the number of electrons. In panel (f), the $a = 4$ curve has a MAE of 6×10^{-3} , 2×10^{-3} , 4×10^{-3} at $N_e = 18, 24, 30$, respectively. Finally, it is worth noting that the extrapolation of the functional (both energy density and potential) does not seem to have a strong dependence on the degree of non-locality.

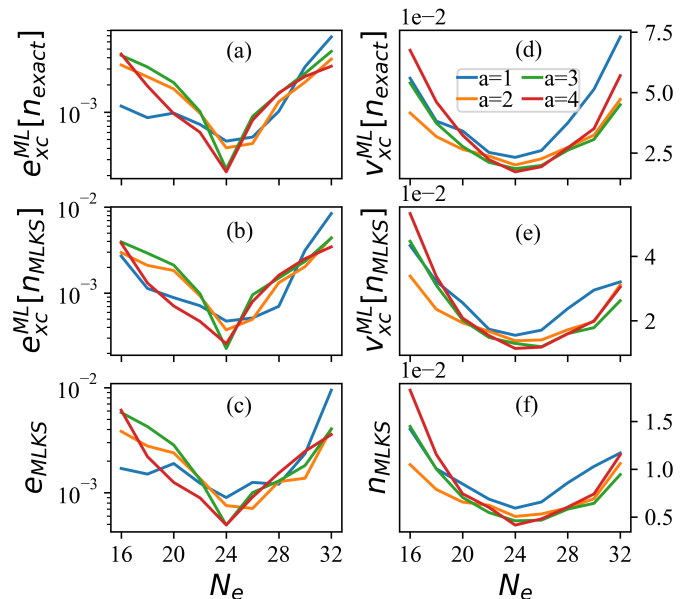


FIG. 6. MAE obtained over 128 disordered configurations for the exchange-correlation energy density and KS potential of a system of 36 sites and different number of electrons, N_e . The model has been trained at $N_e = 24$, where the highest accuracy is reached. The various quantities have been defined in the main text.

The success of the model's extrapolation is likely due to the inhomogeneous nature of the training data, combined with the semi-local architecture of the functional. This gives the model exposure to density regions with occupations both higher and lower than $2/3$ filling. It can be expected that this extrapolation (the functional accuracy) will improve as the system size is increased, provided that only a few electrons are added to the system, since $(N_e \pm \delta N_e)/L \approx N_e/L$ for large L (namely for variations close to the training range). The ability of the model to extrapolate is a useful property, as it allows one to perform tests, which require N_e to be varied. For instance, one could compute the band gap, or the inverse compressibility [52, 53]. In particular, in the next section III D, we test whether or not the KS energy is piecewise linear.

D. Piecewise Linearity of the KS energy

Conventional DFT can be extended to fractional numbers of electrons by using a zero-temperature ensemble of integer electron states. Within this framework, it can be shown that the exact DFT total energy computed at integer electron-number values connects linearly [54], namely the $E - N_e$ curve is piecewise linear. This property formally writes

$$E(N) = (1 - x)E(N_0) + xE(N_0 + 1), \quad (13)$$

where $N = N_0 + x$, N_0 is an integer and x is taken in the interval $[0, 1]$. The piecewise linearity, however, is not satisfied by semi-local density functionals [55–62]. For instance, in the local density approximation such curve is approximately parabolic around the neutrality point. The shortfall is widely attributed to the ‘delocalization error’ or the related ‘self-interaction error’, which gives rise to a set of hallmark DFT deficiencies: an inaccurate description of charge transfer and charge distribution in separated systems, a systematic under-estimation of the band gaps, and generally over delocalized orbitals [63].

If Eq. (13) holds, then the highest occupied Kohn-Sham orbital at $N = N_0$, $\epsilon_{\text{H}}^{N_0}$, is related to the slope of $E(N)$ as

$$\epsilon_{\text{H}}^{N_0} = \frac{\partial E}{\partial N} = E(N_0) - E(N_0 - 1), \quad (14)$$

so that $-\epsilon_{\text{H}}^{N_0}$ equals the ionization potential, IP . The same argument can then be applied to the case of $N_0 + 1$ electrons, where one finds the electron affinity, EA , of the N_0 electron system. Thus, one can conclude that the fundamental gap of a molecule containing N_0 electrons is simply

$$\Delta^{N_0} = IP - EA = \lim_{x \rightarrow 0} \left\{ \left. \frac{\partial E}{\partial N} \right|_{N_0+x} - \left. \frac{\partial E}{\partial N} \right|_{N_0-x} \right\}. \quad (15)$$

In general, Δ^{N_0} is not the difference between the lowest-unoccupied and the highest-occupied Kohn-Sham orbital (the Kohn-Sham gap), $\Delta_{\text{KS}}^{N_0} = \epsilon_{\text{L}}^{N_0} - \epsilon_{\text{H}}^{N_0}$, a fact attributed to the lack of derivative discontinuity of the exchange-correlation energy.

We now test both the MLKS functional (we focus here only on the $a = 4$ case) and the BALDA against this behaviour for a homogeneous $L = 36$ lattice, which can be viewed as a large molecule. In the upper panel of Fig. 7 we present the total energy as a function of the number of electrons, while the lower panel shows its derivative. The exact limit is established by the DMRG results. In this case we have access only to integer values of the electron number and the energy, by construction, is piecewise linear at any integer. In contrast, the total energy of both the MLKS functional and the BALDA changes slope only at even electron numbers, while in between those the $E(N_e)$ curve is convex. This is because the

MLKS functional has been trained only for the $N_{\uparrow} = N_{\downarrow}$ case and we do not have access to broken symmetry solutions. Note that in standard DFT the exact functional should satisfy the flat-plane condition with respect to the magnetization [64, 65], so that one does not need a broken symmetry solution to satisfy the derivative discontinuity at odd electron count. In our case the MLKS functional has never experienced any configurations with an odd number of electrons, so that the highest occupied Kohn-Sham orbital is continuously filled until it accommodates two electrons under the constrain $N_{\uparrow} = N_{\downarrow}$. This gives rise to a linear dependence of the energy derivative (see lower panel of Fig. 7). Such dependence is only partially satisfied for $N_0 < 24$, probably due to some numerical error.

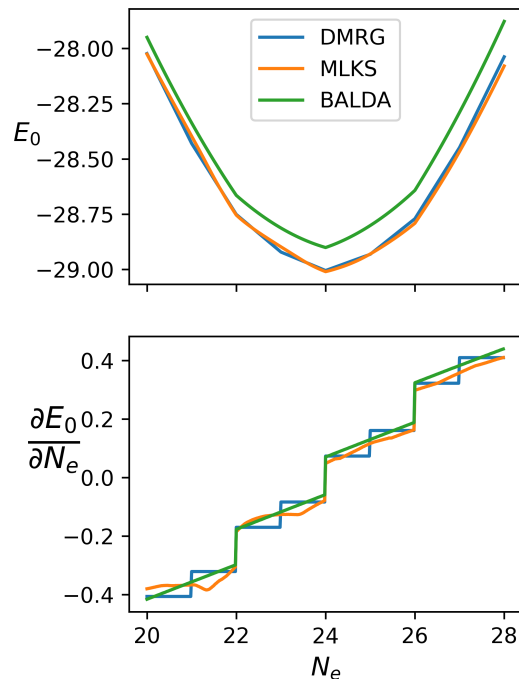


FIG. 7. Total energy against the number of electrons (top panel) and its derivative (bottom panel) for different functionals. Results are presented for a homogeneous $L = 36$ lattice. The blue curves (DMRG) are computed by DMRG at integer electron numbers and interpolated linearly using Eq. (13). The BALDA and MLKS curves are computed by solving the Kohn-Sham equations at fractional occupation. In the case of MLKS we have used the functional with $a = 4$.

The linearity of $\frac{\partial E}{\partial M}$ between even integers implies that in that interval the Kohn-Sham energy is parabolic with the electron filling. This means that the Hartree contribution to the total energy, $E_{\text{H}} = \frac{U}{4} \sum_i n_i^2$, is not compensated by the curvature of the exchange-correlation energy (here we refer to the conventional definition of exchange-correlation energy, since the exchange-correlation energy of the MLKS functional contains the Hartree term). The persistence of this error through the BALDA and the MLKS functional is thus inherent to (semi-) local func-

TABLE I. System gap computed at even-integer electron numbers, N_0 . In the table we report the DMRG gap, $\Delta_{\text{DMRG}}^{N_0}$, the LDFT one computed from Eq. (15), $\Delta_{\text{app}}^{N_0}$, and the Kohn-Sham gap, $\Delta_{\text{KS}}^{N_0}$. In addition we report the corresponding percentage errors, $\delta_{\text{app}}^{N_0}$ and $\delta_{\text{KS}}^{N_0}$, respectively. Data correspond to those presented in Fig. 7 for a homogeneous $L = 36$ lattice.

N_0	DMRG			MLKS			BALDA		
	$\Delta_{\text{DMRG}}^{N_0}$	$\Delta_{\text{app}}^{N_0}$	$\delta_{\text{app}}^{N_0}$ (%)	$\Delta_{\text{KS}}^{N_0}$	$\delta_{\text{KS}}^{N_0}$ (%)	$\Delta_{\text{app}}^{N_0}$	$\delta_{\text{app}}^{N_0}$ (%)	$\Delta_{\text{KS}}^{N_0}$	$\delta_{\text{KS}}^{N_0}$ (%)
22	0.151	0.121	20.3	0.127	16.1	0.122	19.1	0.127	15.8
24	0.157	0.127	19.4	0.135	13.7	0.130	17.4	0.138	12.0
26	0.162	0.135	16.3	0.144	10.8	0.136	15.5	0.142	12.0
28	0.164	0.141	13.9	0.148	10.1	0.142	13.7	0.149	9.1

tionals, as is the case in *ab-initio* DFT.

To conclude this section we verify the accuracy of the constructed functional at describing the system gap, as defined in Eq. (15). In this case we have access to the exact DMRG result, $\Delta_{\text{DMRG}}^{N_0}$, and to the LDFT values, $\Delta_{\text{app}}^{N_0}$. The comparison is carried out only at even integers where the LDFT gaps are defined, with the results presented in Table I. In particular, together with $\Delta_{\text{app}}^{N_0}$ we also report the computed Kohn-Sham gap, $\Delta_{\text{KS}}^{N_0}$, and the corresponding percentage errors, $\delta_{\alpha}^{N_0} (\Delta_{\text{DMRG}}^{N_0} - \Delta_{\alpha}^{N_0}) / \Delta_{\text{DMRG}}^{N_0}$, with $\alpha = \text{'app'}$ and 'KS' .

From the table it emerges clear that Δ^{N_0} computed at the LDFT level remains systematically smaller than its corresponding exact DMRG result. In particular, we find little difference between the BALDA and our MLKS functional, both returning an underestimation of the gaps in between 13% and 20%. Importantly, the Kohn-Sham gap, $\Delta_{\text{KS}}^{N_0}$, is quite close to $\Delta_{\text{app}}^{N_0}$, so that the exchange and correlation energy has no derivative discontinuity, both in the case of MLKS and the BALDA. Note that this has not to be confused with the discontinuity that the BALDA presents at half-filling [15], where the functional fits the Mott transition of the uniform infinite 1D Hubbard model.

E. Response to an electric field

In order to demonstrate the use of our ML KS scheme we explore the response of the one-dimensional Hubbard model to an external, constant electric field \mathcal{E} . The response is quantified by the polarizability, α , defined as the derivative of the induced electrical dipole moment, $P(\mathcal{E})$, with respect to the electric field, in the limit $\mathcal{E} \rightarrow 0$. The presence of the electric field adds a linear on-site potential $v_{\mathcal{E}i} = e\mathcal{E}(i - \bar{x})$, which introduces a new term to the Hamiltonian,

$$\hat{H}_{\mathcal{E}} = \sum_{\sigma} \sum_{i=1}^L v_{\mathcal{E}i} \hat{c}_{i\sigma}^{\dagger} \hat{c}_{i\sigma} = e\mathcal{E} \sum_{\sigma} \sum_{i=1}^L (i - \bar{x}) \hat{c}_{i\sigma}^{\dagger} \hat{c}_{i\sigma}, \quad (16)$$

where \bar{x} is the central position in the lattice. The dipole moment can then be computed as the expectation value

of the dipole operator,

$$P(\mathcal{E}) = e \left\langle \Psi_0(\mathcal{E}) \left| \sum_{\sigma} \sum_{i=1}^L (i - \bar{x}) \hat{c}_{i\sigma}^{\dagger} \hat{c}_{i\sigma} \right| \Psi_0(\mathcal{E}) \right\rangle, \quad (17)$$

where $|\Psi_0(\mathcal{E})\rangle$ is the many-body ground-state wavefunction for the given electric field, \mathcal{E} . The same procedure can then be followed by using our ML KS scheme, by solving the self-consistent KS equations in the presence of the electric field term of Eq. (16), and then by computing

$$P(\mathcal{E})^{\text{KS}} = e \sum_{\sigma} \sum_{i=1}^L (i - \bar{x}) n_{i\sigma}^{\text{MLKS}}. \quad (18)$$

The polarizability is then obtained as the numerical derivative of $P(\mathcal{E})$ at $\mathcal{E} = 0$,

$$\alpha = \left. \frac{dP(\mathcal{E})}{d\mathcal{E}} \right|_{\mathcal{E}=0}. \quad (19)$$

1. Polarizability scaling

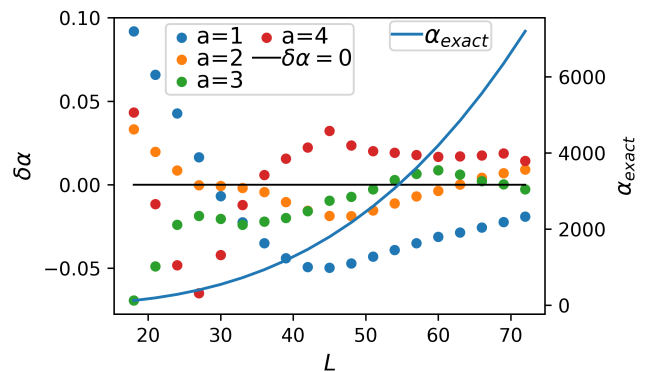


FIG. 8. Polarizability, α , of the 1D Hubbard model at one-third-filling, plotted against the number of sites, L , of a linear open-ended chain. Here α_{exact} is computed with DMRG (blue line - right-hand-side scale), while the symbols show the fractional error, $\delta\alpha = (\alpha_{\text{MLKS}} - \alpha_{\text{exact}}) / \alpha_{\text{exact}}$, of the MLKS-calculated polarizability scheme relative to the exact results (left-hand side y -axis). The calculation is repeated for functionals having different non-locality parameter, a .

Our computed polarizability, α , as a function of the system length, L , is presented in Fig. 8 for homogeneous lattices of size $L = 18, 21, 24, \dots, 72$. In the figure we present the exact DMRG results together with the errors of our ML KS scheme for models constructed with different non-locality parameters. Clearly, there is an excellent agreement between the DMRG and MLKS results across the entire range of lengths, L . The agreement is particularly good for long chains and non-local functionals, and remains always below 5%, except for the small lattices and the $a = 1$ case. This reflects the already noted improvement of the exchange-correlation functional for large systems arising from the reduced relevance of the edge occupations. Furthermore, it is clear that the non-locality improves the quality of the ML KS results, although there is little quantitative difference between different degrees of non-locality.

The polarizability as a function of system size follows a power-law [17] behaviour

$$\alpha(U; L) = \alpha_0 L^\gamma.$$

A numerical fit to the above scaling law [see Fig. 9] yields us exponents $\gamma = 2.851, 2.909, 2.968, 2.956$ for non-locality $a = 1, 2, 3$ and 4, respectively. This is very close to $\gamma = 3$ expected for free electrons in 1D [66] and in line with results obtained with Bethe-ansatz LDFT results [17].

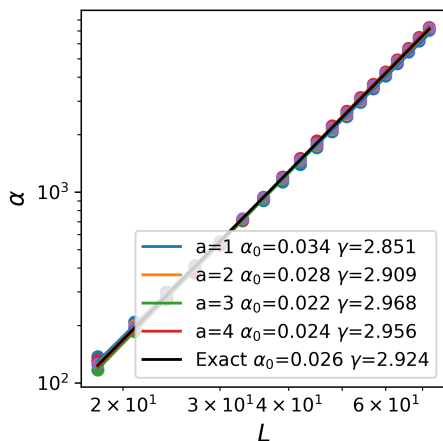


FIG. 9. Polarizability, α versus lattice size, L , plotted on a log-log scale. The legend distinguishes between the various MLKS functionals and the exact results. Also given in the legend are the corresponding values found from fitting the function $\alpha(U; L) = \alpha_0 L^\gamma$.

2. Response of the exchange-correlation potential

In general, in conventional DFT the local and semi-local functionals fail in predicting accurate linear polarizabilities, a feature associated with the incorrect response of the exchange-correlation potential to the electric field.

This failure ultimately boils down to the self-interaction error [67, 68]. Thus, it is important to investigate the response of our ML KS potential to the external field. The exercise can be simply done by plotting the potential response, namely the difference between the potential computed in the presence of a field and without it, $\Delta v = v^\mathcal{E} - v^{\mathcal{E}=0}$, as a function of the site index. At this point, it is useful to separate the classical and non-classical contributions to the exchange-correlation potential, namely to subtract from the v_{xc} previously defined the Hartree component, which is here defined as $(v_H)_i = U n_i / 2$. To keep the notation simple we will keep calling $v_{xc} - v_H$ as v_{xc} .

In Fig. 10 we then plot Δv_H , Δv_{xc} and $\Delta v_\mathcal{E}$, where $v_\mathcal{E}$ is the potential associated to the electric field [see Eq. (16)]. Results are presented for a system of $L = 48$ sites and for the ML functional with $a = 3$, which has returned the most accurate polarizability. For completeness we also include results obtained within the BALDA. As usual, we compare the DMRG results (dots) against those obtained with MLKS, showing once again an excellent agreement. As expected the Hartree potential responds against the external one. In contrast, Δv_{xc} has the same slope of $\Delta v_\mathcal{E}$. This behaviour is opposite to what found for *ab initio* DFT, but it is consistent with previous Bethe-ansatz LDFT results [17], as confirmed numerically here as well. In order to quantify the potential response, we compute for each of the potentials the product, $\sum_i \Delta v_i \cdot (i - \bar{x})$, which we refer to as $\Delta v \cdot \vec{r}$ and describes the slope of the response. With this definition at hand, we conclude that the Hartree response is about ten-fold larger than the exchange-correlation ones. It is also worth to note that the results obtained with our ML functional are close to those obtain with the BALDA, indicating that at least for this quantity the non-locality does not seem to play a key role.

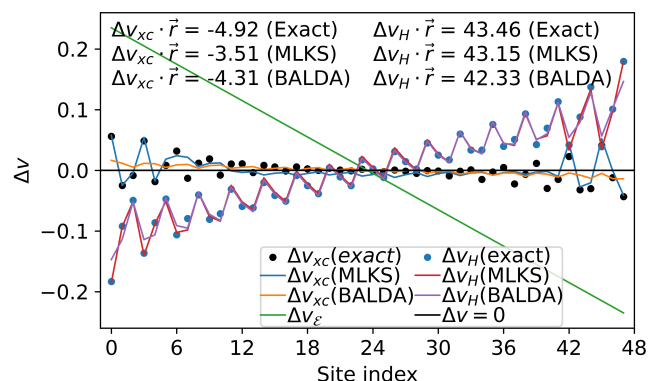


FIG. 10. Response of the Hartree and exchange-correlation potential to the external electrostatic potential, plotted against the site index for a homogeneous $L = 48$ lattice. For the MLKS calculations we use the $a = 3$ functional. A measure of the response can be obtained from $\Delta v \cdot \vec{r}$ (see text), whose values are reported in the legends.

3. Polarizability for disordered systems as they approach the thermodynamics limit

One of the major advantages of a MLKS scheme is that it can be applied to any system size and distribution of on-site energies (within the range of the training data). As such, it is ideal to investigate the effect of disorder as the system approaches the thermodynamic limit, an exercise performed here for the polarizability. Our analysis starts with systems comprising 21 and 42 sites, which are accessible by DMRG. For both system sizes, we generate $n = 2000$ random disorder configurations from $v_i^{(k)} \in [-\lambda^{(k)}, \lambda^{(k)}]$ where $\lambda^{(k)} = 3k/2(n-1)$. Then, we compute and plot the polarizability against a one-dimensional measure of the disorder, namely the absolute variance $\delta v = \frac{1}{L} \sum_i^L |v_i|$ (note that each disorder configuration has zero mean).

The results are shown in the Fig. 11, where we present the polarizability for all the 2,000 configurations, computed with DMRG and with the KS schemes, either using our ML functional ($a = 4$) or the BALDA. Clearly, our MLKS-computed polarizabilities are in close agreement with the exact DMRG results across the entire range of disorder investigated. In contrast, the BALDA provides good polarizabilities for weak disorder but tends to drastically under-estimate the spread of the distribution for high disorder. This is the situation where the site occupations may distribute over a larger range. It is also clear that the distributions of α as a function of δv are different for systems of different size, namely they are less diffused for long chains. We will return on this point when analysing the limit of large chains.

For our large-scale investigation, we examine systems containing respectively $L = 21, 42, 84, 168, 336, 672$ and 1344 sites. In this case we consider only four different levels of disorder, namely $\delta v = 0.05, 0.1, 0.2, 0.4$. For each L and δv we generate 200 random disorder configurations and rescale the on-site energies so to return the required δv value. The polarizability is then computed according to Eq. (19) with a finite difference of $\mathcal{E} = 1/2L$. For this scaling exercise we monitor the relative change in the average polarizability with respect to that of the homogeneous system, α_0 , namely

$$R_{\text{avg}}(\delta v, L) = \frac{\alpha_{\text{avg}}(\delta v, L) - \alpha_0}{\alpha_0}, \quad (20)$$

while the distribution of the data is analysed by computing the 2.5th and 97.5th percentiles.

For these system sizes we no longer have access to DMRG results, so that we limit the comparison of our MLKS results to those obtained with BALDA and to the non-interacting case. In Fig. 12 we present $R_{\text{avg}}(\delta v, L)$ against length for different levels of disorder and the different models used. A few key points must be noticed. Firstly, in all cases the average polarizability remains close to that computed for the homogeneous case at the same level of theory. In the non-interacting case, at low disorder, the individual polarizabilities computed for

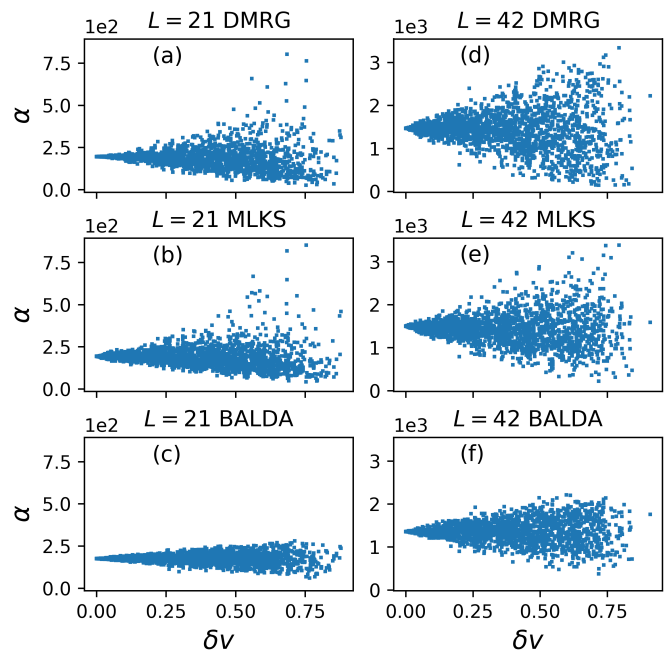


FIG. 11. The polarizability, α , against disorder strength, $\delta v = \frac{1}{L} \sum_i^L |v_i|$, computed with DMRG (top row), MLKS (middle row) and BALDA (bottom row), for systems of $L = 21$ lattice sites (left column) and $L = 42$ (right column). In each subplot we show data for 2,000 disorder configurations. In the case of MLKS, we use the model trained with non-locality $a = 4$.

different configurations distribute symmetrically about the average, a symmetry that breaks down for large δv . Overall then, the spread of $R_{\text{avg}}(\delta v, L)$ values reduces monotonically with the system size, suggesting that in the thermodynamic limit (infinite L) one should expect the polarizability to be that of the homogeneous case.

When Coulomb repulsion is switched on (finite U) both our MLKS and the BALDA scheme return us a polarizability spread significantly smaller than that of the non-interacting case. This is not surprising since the Coulomb repulsion is more pronounced in regions of high density, so that for the same on-site energy random arrangement one expects the interacting problem to yield a more homogeneous charge density. In turn, this reduces the deviation of the computed polarizability from their average. This effect can be quantified by looking at the difference between the 97.5th and the 2.5th percentile of the distribution for the largest chain, $L = 1,344$, and strongest disorder, $\delta v = 0.4$. This is 0.1 for both MLKS and BALDA and 0.37 for the non-interacting case.

Finally, we wish to take a closer look at the dependence of the average polarizability as a function of the disorder strength. As noted before, this eventually approaches the homogeneous-chain limit, but for finite chains a small dependence is noticed. As this is difficult to extract from the plots in Fig. 12 due to the scale, in Fig. 13 we present the deviation of the average α from the homogeneous case

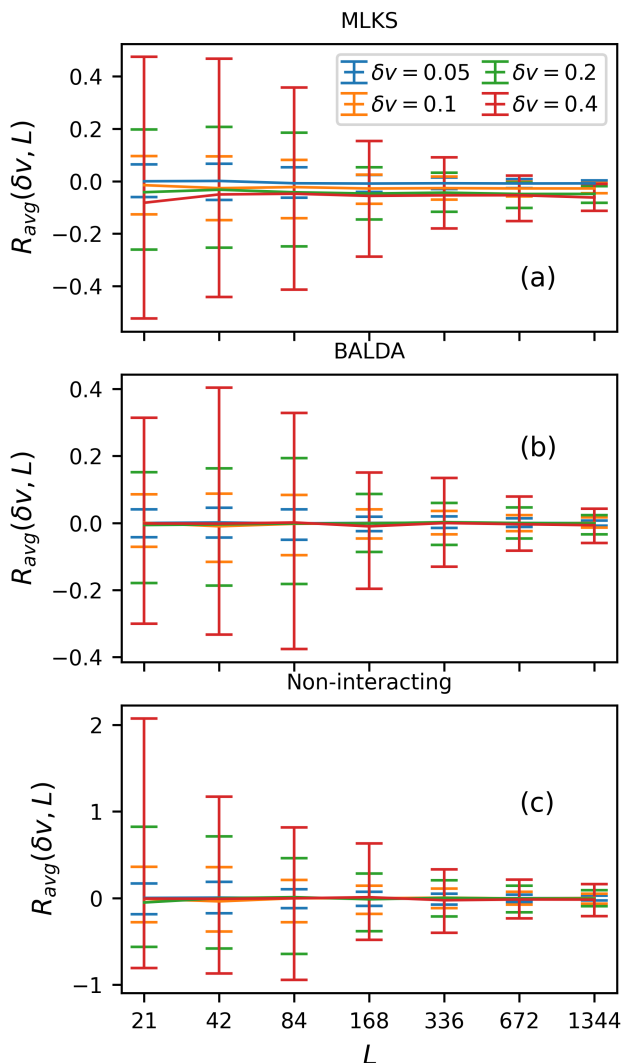


FIG. 12. Relative change in the averaged polarizability, $R_{\text{avg}}(\delta v, L)$ as a function of the lattice size L , for different levels of disorder δv . The lower (upper) error bars give the 2.5th (97.5th) percentile of the distribution. Panels (a), (b) and (c) show the results from MLKS, BALDA and the non-interacting tight-binding model, respectively. There are 200 data points for each $(L, \delta v)$ pair. For the MLKS scheme, we use the model trained with non-locality $a = 4$.

as a function of δv for a 21-site-long chain and the different models. In constructing the graph we have averaged over a different number of samples, so that the variance of the different methods is approximately similar (the average is equally statistically significant). Clearly the deviation from the homogeneous limit, as expected, increases with the disorder strength. Such an increase is underestimated by both BALDA and by the non-interacting tight-binding model, but it is well captured by our MLKS scheme, which remains close to the DMRG results at all δv .

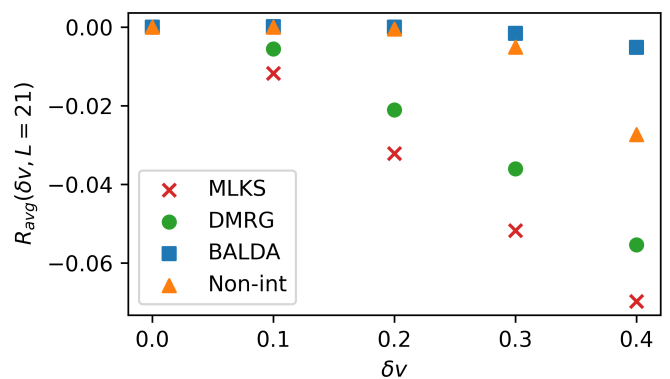


FIG. 13. R_{avg} against disorder strength, $\delta v = 0.1, 0.2, 0.3, 0.4$, for a chain containing 21 sites, computed at different levels of theory. For each δv we average over $n = 16,00$ disorder configurations for MLKS and DMRG, and over $n = 51,200$ for BALDA and the non-interacting case. This returns approximately the same variance.

IV. CONCLUSION AND OUTLOOK

We have presented a method for the construction of a ML energy functional for the one-dimensional Hubbard model, which can define a Kohn-Sham potential by functional derivative. This enables us to use Kohn-Sham DFT for a lattice model, with an accuracy comparable to that of DMRG, which is used to generate the training set. In particular, we construct a class of functionals with different degree of non-locality. These can be trained on systems with moderate size and deployed for much larger ones. In general, we find that the accuracy of the functional improves with the degree of non-locality and that most of the error concentrates on lattice sites at the edge of the linear molecules. These present charge distribution unevenly represented in the training set, so that the error has to be considered numerical. All constructed functionals perform significantly better than the Bethe-Ansatz local density approximation (BALDA), often used for the DFT of the Hubbard model.

Since the computational costs of our MLKS functionals are similar to that of the BALDA and scale with the number of sites, the method can be used to investigate large systems and/or situations where ensemble averages are important. For this reason, we have looked at the electrical polarizability of both homogeneous and disordered linear chain as a function of the chain length and eventually the disorder strength. We find that MLKS can return polarizability values in close agreement to DMRG results and, in the case of disorder, a very similar spread in their distributions. This is not the case of the BALDA, which tends to under-estimate the spreads. In any case, we find that the polarizability of disordered systems converges to that of the homogeneous case as the system size is increased and that the convergence is faster for the interacting case.

The method presented here still presents some limita-

tions. Firstly, the functionals are defined for a specific value of U/t , so that different Coulomb strengths will require a new parametrization. In principle, one could train a single model to work with a range of model parameters $\{U_i, t_{ij}\}$, which effectively would act as a ‘collection’ of functionals. Alternatively, one can move to density matrix functional theory, where the fundamental quantity becomes the single-particle density matrix, but one has access to a more general definition of kinetic energy [69]. A second limitation is that here the models have been trained specifically for the 2/3 filling case. Although we have shown that the functionals are transferable to different, although close, filling factors, it is reasonable to expect that our semi-local approximation will break down as the model correlation length diverges. The Mott-insulator phase transition of the one-dimensional Hubbard model at half filling is one such case. Despite the limitations, it appears that our MLKS scheme can still be useful to explore similar models of relevance either at fundamental level or for possible applications in materials science. For instance, the extension to higher dimensions is in reach and only limited by our ability to generate exact results for the training. Also intriguing is the possibility to extend our construction to the canonical ensemble [36] and to bosonic degrees of freedom [70]. One can then investigate phenomena such as superconductivity or polaron formation and transport.

ACKNOWLEDGMENTS

We would like to thank Akinlolu Akande for insightful discussions regarding the BALDA and DMRG. This work has been funded by the Irish Research Council through a PhD scholarship (E.C.) (Grant No. GOIPG/2021/715). We acknowledge Trinity Centre for High Performance Computing (TCHPC) for the provision of computational resources. We acknowledge the use of GPU’s provided by the Nvidia Academic Hardware grant.

Appendix A: Machine-learning the local functional

In Section III A we have examined the parity plots of both the $a = 4$ functional as well as the BALDA. It is interesting to see how well the ML fully-local, $a = 0$, functional compares to the BALDA. Thus, we perform the same test as in Section III A, however with $a = 0$ instead of $a = 4$. The results are given in Fig. 14. It is interesting to see that when the ML model is reduced from a semi-local functional to a fully local one, it acquires some of the same systematic errors that are displayed by the BALDA. The $a = 0$ MLKS returns lower MAE’s for each of the six quantities [panels (a) through (f)]. This can be understood as follows. The BALDA is a functional that is exact in the case of the infinite homogeneous 1D chain

for any given value of the filling, whereas the $a = 0$ is a local model that relates an input density to an energy, that is optimized to be most accurate for the systems in the training set (2/3 filling). In fact, any discrepancy between the BALDA and the MLKS $a = 0$ functional implies that the latter does not recover the correct infinite limit of the homogeneous electron density.

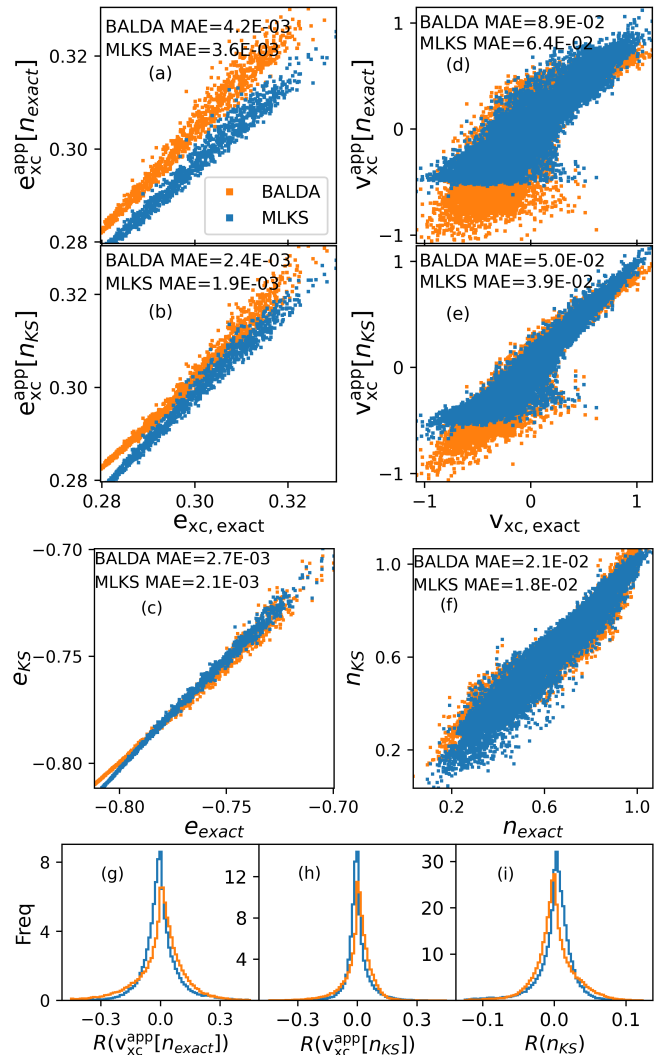


FIG. 14. Analysis of the accuracy of the KS ML functional. For a system $L = 60$ we present the parity plot of both the ML fully-local, $a = 0$, functional compares to the BALDA. Thus, we perform the same test as in Section III A, however with $a = 0$ instead of $a = 4$. The results are given in Fig. 14. It is interesting to see that when the ML model is reduced from a semi-local functional to a fully local one, it acquires some of the same systematic errors that are displayed by the BALDA. The $a = 0$ MLKS returns lower MAE’s for each of the six quantities [panels (a) through (f)]. This can be understood as follows. The BALDA is a functional that is exact in the case of the infinite homogeneous 1D chain

-
- [1] P. Hohenberg and W. Kohn, *Inhomogeneous electron gas*, Phys. Rev. **136**, B864 (1964).
- [2] W. Kohn and L.J. Sham, *Self-consistent equations including exchange and correlation effects*, Phys. Rev. **140**, A1133 (1965).
- [3] K. Lejaeghere et al., Reproducibility in density functional theory calculations of solids, *Science* **2016**, 351, aad3000.
- [4] W. Mi, K. Luo, S.B. Trickey and M. Pavanello, *Orbital-Free Density Functional Theory: An Attractive Electronic Structure Method for Large-Scale First-Principles Simulations*, Chem. Rev. **123**, 12039 (2023).
- [5] J. P. Perdew and K. Schmidt, *Jacob's ladder of density functional approximations for the exchange-correlation energy*, AIP Conf. Proc. **577**, 1 (2001).
- [6] P. Mori-Sánchez, A.J. Cohen and W.T. Yang, *Discontinuous Nature of the Exchange-Correlation Functional in Strongly Correlated Systems*, Phys. Rev. Lett. **102**, 066403 (2009).
- [7] O. Gunnarsson and K. Schönhammer, *Density-Functional Treatment of an Exactly Solvable Semiconductor Model*, Phys. Rev. Lett. **56**, 1968 (1986).
- [8] K. Schönhammer, O. Gunnarsson and R.M. Noack, *Density-functional theory on a lattice: Comparison with exact numerical results for a model with strongly correlated electrons*, Phys. Rev. B **52**, 2504 (1995).
- [9] J. Hubbard, *Electron correlations in narrow energy bands III. An improved solution*, Proc. R. Soc. Lond. A **281**, 401 (1964).
- [10] K. Capelle and V.L. Campo Jr., *Density functionals and model Hamiltonians: Pillars of many-particle physics*, Phys. Rep. **528**, 91 (2013).
- [11] V.V. França, J.P. Coe and I. D'Amico, *Testing density-functional approximations on a lattice and the applicability of the related Hohenberg-Kohn-like theorem*, Sci. Rep. **8**, 664 (2018).
- [12] M. Penz and R van Leeuwen, *Density-Functional Theory on Graphs*, J. Chem. Phys. **155**, 244111 (2021).
- [13] N. Sobrino, D. Jacob and S. Kurth, *What can lattice DFT teach us about real-space DFT?*, J. Chem. Phys. **159**, 154110 (2023).
- [14] F.H.L. Essler, H. Frahm, F. Göhmann, A. Klümper and V.E. Korepin, *the one-dimensional Hubbard model*, Cambridge University Press, Cambridge 2005.
- [15] N.A. Lima, L.N. Oliveira and K. Capelle, *Density-functional study of the Mott gap in the Hubbard model*, Europhys. Lett. **60**, 601 (2002).
- [16] N.A. Lima, M.F. Silva, L.N. Oliveira and K. Capelle, *Density functionals not based on the electron gas: Local-density approximation for a Luttinger liquid*, Phys. Rev. Lett. **90**, 146402 (2003).
- [17] A. Akande and S. Sanvito, *Electric field response of strongly correlated one-dimensional metals: A Bethe ansatz density functional theory study*, Phys. Rev. B **82**, 245114 (2010).
- [18] A. Akande and S. Sanvito, *Persistent current and Drude weight for the one-dimensional Hubbard model from current lattice density functional theory*, J. Phys.: Condens. Matter **24**, 099601 (2012).
- [19] S. Schenk, M. Dzierzawa, P. Schwab and U. Eckern, *Successes and failures of Bethe ansatz density functional theory*, Phys. Rev. B **78**, 165102 (2008).
- [20] V.V. França, D. Vieira and K. Capelle, *Simple parameterization for the ground-state energy of the infinite Hubbard chain incorporating Mott physics, spin-dependent phenomena and spatial inhomogeneity*, New J. Phys. **14**, 073021 (2012).
- [21] V. Vettchinkina, A. Kartsev, D. Karlsson and C. Verdozzi, *Interacting fermions in one-dimensional disordered lattices: Exploring localization and transport properties with lattice density-functional theories*, Phys. Rev. B **87**, 115117 (2013).
- [22] J.C. Snyder, M. Rupp, K. Hansen, K.-R. Müller and K. Burke, *Finding Density Functionals with Machine Learning*, Phys. Rev. Lett. **108**, 253002 (2012).
- [23] L. Li, J. C. Snyder, I. M. Pelaschier, J. Huang, U.-N. Niranjan, P. Duncan, M. Rupp, K.-R. Müller and K. Burke, *Understanding machine-learned density functionals*, Int. J. Quantum Chem. **116**, 819 (2016).
- [24] L. Li, T. E. Baker, S. R. White, and K. Burke, *Pure density functional for strong correlation and the thermodynamic limit from machine learning*, Phys. Rev. B **94**, 245129 (2016).
- [25] K. Mills, M. Spanner and I. Tamblyn, *Deep learning and the Schrödinger equation*, Phys. Rev. A **96**, 042113 (2017).
- [26] J. Schmidt, C.L. Benavides-Riveros and M.A.L. Marques, *Machine Learning the Physical Nonlocal Exchange-Correlation Functional of Density-Functional Theory*, J. Phys. Chem. Lett. **10**, 6425 (2019).
- [27] K. Ryczko, D. A. Strubbe and I. Tamblyn, *Deep learning and density-functional theory*, Phys. Rev. A **100**, 022512 (2019).
- [28] B. Kalita, L. Li, R.J. McCarty and K. Burke, *Learning to Approximate Density Functionals*, Acc. Chem. Res. **54**, 818 (2021).
- [29] L. Zepeda-Núñez, Y. Chen, J. Zhang, W. Jia, L. Zhang and L. Lin, *Deep Density: Circumventing the Kohn-Sham equations via symmetry preserving neural networks*, J. Comp. Phys. **443**, 110523 (2021).
- [30] F. Brockherde, L. Vogt, L. Li, M.E. Tuckerman, K. Burke and K.-R. Müller, *Bypassing the Kohn-Sham equations with machine learning*, Nature Commun. **24**, 872 (2017).
- [31] B. Focassio, M. Domina, U. Patil, A. Fazzio and S. Sanvito, *Linear Jacobi-Legendre expansion of the charge density for machine learning-accelerated electronic structure calculations*, npj Comput **9**, 87 (2023).
- [32] B. Focassio, M. Domina, U. Patil, A. Fazzio and S. Sanvito, *Covariant Jacobi-Legendre expansion for total energy calculations within the projector augmented wave formalism*, Phys. Rev. B **110**, 184106 (2024).
- [33] J.R. Moreno, G. Carleo and A. Georges, *Deep Learning the Hohenberg-Kohn Maps of Density Functional Theory*, Phys. Rev. Lett. **125**, 076402 (2020).
- [34] J.R. Moreno, J. Flick and A. Georges, *Machine learning band gaps from the electron density*, Phys. Rev. Mater. **5**, 083802 (2021).
- [35] J. Nelson, R. Tiwari and S. Sanvito, *Machine learning density functional theory for the Hubbard model*, Phys. Rev. B **99**, 075132 (2019).
- [36] J. Nelson, R. Tiwari and S. Sanvito, *Machine-learning semilocal density functional theory for many-body lattice models at zero and finite temperature*, Phys. Rev. B **103**,

- 245111 (2021).
- [37] S.R. White, *Density matrix formulation for quantum renormalization groups*, Phys. Rev. Lett. **69**, 2863 (1992).
- [38] J. Hauschild and F. Pollmann, *Efficient numerical simulations with Tensor Networks: Tensor Network Python (TeNPy)*, SciPost Phys. Lect. Notes **5** (2018).
- [39] Y. Shi and A. Wasserman, *Inverse Kohn-Sham Density Functional Theory: Progress and Challenges*, J. Phys. Chem. Lett. **12**, 5308 (2021).
- [40] C.G. Broyden, *The Convergence of a Class of Double-rank Minimization Algorithms 1. General Considerations*, IMA J. Appl. Math. **6**, 76 (1970).
- [41] R. Fletcher, *A new approach to variable metric algorithms*, Comput. J. **13**, 317 (1970).
- [42] D. Goldfarb, *A family of variable-metric methods derived by variational means*, Math. Comput. **24**, 23 (1970).
- [43] D.F. Shanno, *Conditioning of quasi-Newton methods for function minimization*, Math. Comput. **24**, 647 (1970).
- [44] P. Virtanen et al., *SciPy 1.0: Fundamental Algorithms for Scientific Computing in Python*, Nat. Methods **17**, 261 (2020).
- [45] <https://github.com/eoghancronin/ml-ldft>
- [46] M. Abadi et al., *TensorFlow: Large-Scale Machine Learning on Heterogeneous Systems*, in OSDI'16: Proceedings of the 12th USENIX conference on Operating Systems Design and Implementation, (2016).
- [47] L.O. Wagner, E.M. Stoudenmire, K. Burke and S.R. White, *Guaranteed Convergence of the Kohn-Sham Equations*, Phys. Rev. Lett. **111**, 093003 (2013).
- [48] H. Shiba, *Magnetic Susceptibility at Zero Temperature for the One-Dimensional Hubbard Model*, Phys. Rev. B **9**, 930 (1972).
- [49] The GitHub repository that we used to solve the coupled integral equations of the Bethe-Ansatz is available at github.com/sunchong137/BetheAnsatz and was developed alongside Refs. [50, 51]:
- [50] G. Knizia, G. K. L. Chan, *Density Matrix Embedding: A Simple Alternative to Dynamical Mean-Field Theory*, Phys. Rev. Lett. **109**, 186404 (2012).
- [51] S. Chong, U. Ray, Z.H. Cui, M. Stoudenmire, M. Ferrero, G. K. L. Chan, *Finite-temperature density matrix embedding theory*, Phys. Rev. B **101**, 075131 (2020).
- [52] F. Mila, X. Zotos, *Phase Diagram of the One-Dimensional Extended Hubbard Model at Quarter-Filling*, Europhys. Lett. **24**, 133 (1993).
- [53] G. Xianlong, M. P. Polini, M. P. Tosi, V. L. Campo Jr., K. Capelle, and M. Rigol, *Bethe ansatz density-functional theory of ultracold repulsive fermions in one-dimensional optical lattices*, Phys. Rev. B **73**, 165120 (2006).
- [54] J. P. Perdew, R. G. Parr, M. Levy, and J. L. Balduz, *Density-Functional Theory for Fractional Particle Number: Derivative Discontinuities of the Energy*, Phys. Rev. Lett. **49**, 1691 (1982).
- [55] P. Mori-Sánchez, A. J. Cohen, and W. Yang, *Many-electron self-interaction error in approximate density functionals*, J. Chem. Phys. **125**, 201102 (2006).
- [56] T. Stein, J. Autschbach, N. Govind, L. Kronik, and R. Baer, *Curvature and Frontier Orbital Energies in Density Functional Theory*, J. Phys. Chem. Lett. **3**, 3740 (2012).
- [57] A. J. Cohen, P. Mori-Sánchez, and W. Yang, *Insights into Current Limitations of Density Functional Theory*, Science **321**, 792 (2008).
- [58] A. Ruzsinszky, J. P. Perdew, G. I. Csonka, O. A. Vydrov, and G. E. Scuseria, *Density functionals that are one- and two- are not always many-electron self-interaction-free, as shown for H_2^+ , He_2^+ , LiH^+ , and Ne_2^+* , J. Chem. Phys. **126**, 104102 (2007).
- [59] O. A. Vydrov, G. E. Scuseria, and J. P. Perdew, *Tests of functionals for systems with fractional electron number*, J. Chem. Phys. **126**, 154109 (2007).
- [60] R. Haunschild, T. M. Henderson, C. A. Jiménez-Hoyos, and G. E. Scuseria, *Many-electron self-interaction and spin polarization errors in local hybrid density functionals*, J. Chem. Phys. **133**, 134116 (2010).
- [61] A. J. Cohen, P. Mori-Sánchez, and W. Yang, *Challenges for Density Functional Theory*, Chem. Rev. **112**, 289 (2012).
- [62] E. Kraisler, L. Kronik, *Piecewise Linearity of Approximate Density Functionals Revisited: Implications for Frontier Orbital Energies*, Phys. Rev. Lett. **110**, 126403 (2013).
- [63] R. Armiento, S. Kümmel, *Orbital Localization, Charge Transfer, and Band Gaps in Semilocal Density-Functional Theory*, Phys. Rev. Lett. **111**, 036402 (2013).
- [64] W. Yang, Y. Zhang and P. W. Ayers, *Degenerate Ground States and a Fractional Number of Electrons in Density and Reduced Density Matrix Functional Theory*, Phys. Rev. Lett. **84**, 5172 (2000).
- [65] A. J. Cohen, P. Mori-Sánchez and W. Yang, *Fractional spins and static correlation error in density functional theory*, J. Chem. Phys. **129**, 121104 (2008).
- [66] A.G. Rojo and G.D. Mahan, *Nonlinear polarizability of correlated one-dimensional systems*, Phys. Rev. B **47**, 1794 (1993).
- [67] T. Körzdörfer, M. Mundt and S. Kümmel, *Electrical Response of Molecular Systems: The Power of Self-Interaction Corrected Kohn-Sham Theory*, Phys. Rev. Lett. **100**, 133004 (2008).
- [68] C.D. Pemmaraju, S. Sanvito and K. Burke, *Polarizability of molecular chains: A self-interaction correction approach*, Phys. Rev. B **77**, 121204R (2008).
- [69] R. López-Sandoval and G.M. Pastor, *Density-matrix functional theory of the Hubbard model: An exact numerical study*, Phys. Rev. B **61**, 1764 (2000).
- [70] E. V. Bostrom, P. Helmer, P. Werner and C. Verdozzi, *Electron-electron versus electron-phonon interactions in lattice models: Screening effects described by a density functional theory approach*, Phys. Rev. Res **1**, 013017 (2019).